Dynamic Potential Vorticity Initialization and the Diagnosis of Mesoscale Motion

ÁLVARO VIÚDEZ

Institut de Ciències del Mar, Barcelona, Spain

DAVID G. DRITSCHEL

Mathematical Institute, University of St Andrews, St Andrews, United Kingdom

(Manuscript received 29 July 2003, in final form 2 June 2004)

ABSTRACT

A new method for diagnosing the balanced three-dimensional velocity from a given density field in mesoscale oceanic flows is described. The method is referred to as dynamic potential vorticity initialization (PVI) and is based on the idea of letting the inertia–gravity waves produced by the initially imbalanced mass density and velocity fields develop and evolve in time while the balanced components of these fields adjust during the diagnostic period to a prescribed initial potential vorticity (PV) field. Technically this is achieved first by calculating the prescribed PV field from given density and geostrophic velocity fields; then the PV *anomaly* is multiplied by a simple time-dependent ramp function, initially zero but tending to unity over the diagnostic period. In this way, the PV anomaly builds up to the prescribed anomaly. During this time, the full three-dimensional primitive equations—except for the PV equation—are integrated for several inertial periods. At the end of the diagnostic period the density and velocity fields are found to adjust to the prescribed PV field and the approximate balanced vortical motion is obtained. This adjustment involves the generation and propagation of fast, small-amplitude inertia–gravity waves, which appear to have negligible impact on the final near-balanced motion. Several practical applications of this method are illustrated. The highly nonlinear, complex breakup of baroclinically unstable currents into eddies, fronts, and filamentary structures is examined. The capability of the method to generate the balanced three-dimensional motion is measured by analyzing the ageostrophic horizontal and vertical velocity—the latter is the velocity component most sensitive to initialization, and one for which a quasigeostrophic diagnostic solution is available for comparison purposes. The authors find that the diagnosed fields are closer to the actual fields than are either the geostrophic or the quasigeostrophic approximations. Dynamic PV initialization thus appears to be a promising way of improving the diagnosis of balanced mesoscale motions.

1. Introduction

The diagnosis of the oceanic velocity field from a measured mass density field is an important and challenging problem in the physics of the ocean. Accurate measurements of the density field over the full depth of the water column are usually easier to obtain than direct measurements of the three-dimensional velocity field. A number of theoretical and numerical methods have been developed to estimate the velocity field, but these generally require specific dynamical conditions to hold. Examples include the classical geostrophic approximation, the quasigeostrophic approximation (QG; see, e.g., Daley 1991, chapter 6), the semigeostrophic approximation (SG; see Eliassen 1948; Hoskins 1975), balance equations (Gent and McWilliams 1983), iterated geostrophic models (Allen 1991), or methods based on the numerical integration of the total three-dimensional balance of momentum [e.g., the digital filter initialization of Lynch and Huang (1992)]. The geostrophic approximation gives estimates only for the horizontal velocity components. The QG and SG approximations filter the relatively fast inertia–gravity waves (IGWs) but may not be accurate enough for strongly ageostrophic processes in mesoscale eddies and fronts. Methods based on the numerical integration of the primitive equations are potentially able to be as exact as the balance of momentum adopted, but they need to deal with three important requirements: 1) minimizing the direct effects of the fast IGWs generated as a result of the initial imbalance between density and velocity fields, but 2) letting the IGWs otherwise develop since they take part in the sought adjustment, while 3) ensuring that the diagnostic density field remains sufficiently close to the initially prescribed one.

Here we introduce a new method to diagnose the velocity field from a given mass density field. The method, referred to as dynamic potential vorticity ini-

Corresponding author address: Dr. Álvaro Viúdez, Institut de Ciències del Mar, P. Marítim 37, 08003-Barcelona, Spain.
E-mail: aviudez@cmima.csic.es

tialization (PVI), provides an adjusted three-dimensional velocity field, which may be regarded as *balanced* in the sense that the amplitude of the IGWs are small—of second-order in the vertical velocity. The approach is based in part on the numerical time integration of the ageostrophic horizontal vorticity over a given diagnostic period. During this integration, IGWs are generated and are able to propagate as in a real-time simulation (requirement 2 above). The density and velocity fields evolve in time but are constrained to be consistent with the prescribed potential vorticity (PV) field at the end of the diagnostic period. This prescribed PV field is calculated from given density and geostrophic velocity fields (e.g., from data); this ensures that the velocity induced by the PV (the *slow motion*) does not advect the density field, which then remains close to its given initial value during the diagnostic period (requirement 3). The generation of IGWs is kept to a minimum (requirement 1) by smoothly ramping up the PV anomaly from zero to the prescribed PV anomaly over the diagnostic period.

Since the PVI is both an initialization and a diagnostic method, it can be used also to initialize the mass density and velocity fields in numerical models for simulation purposes. In this paper we focus on its use as a diagnostic tool, for simplicity. Its use as an initialization tool involves other factors such as whether or not one starts with an exactly known PV field rather than one deduced, as here, from the density data and the associated geostrophic flow.

In the next section we present the mathematical basis of PVI. Section 3 illustrates two moderately realistic examples that are used to assess the utility of PVI for diagnosing the velocity field. The first consists of a baroclinically unstable shear zone developing into a street of anticyclonic eddies, and the second consists of an unstable oceanic jet developing into both cyclonic and anticyclonic eddies.

The analysis of the results is carried out by comparing the actual fields with the PVI diagnosed fields with an emphasis on the ageostrophic motion, particularly on the vertical velocity, since it is the component most sensitive to initialization. The analysis indicates the PVI diagnoses the horizontal and vertical components of the velocity significantly better than either the geostrophic or the QG approximations do. Section 4 closes the paper with a few concluding remarks.

2. Dynamic PV initialization

The key idea of PVI is to let both the density and velocity fields adjust gradually and dynamically, during the diagnostic period, to a prescribed, assumed known, PV field. During this diagnostic period, small-amplitude IGWs are generated that propagate throughout the flow and generally disperse, making possible the adjustment to a nearly balanced state dependent only on the PV field. In this diagnostic application of PVI the only quantity assumed available is the mass density field so that the prescribed PV is the geostrophic PV computed from the geostrophic vorticity.

To avoid the unwanted generation of large-amplitude IGWs during the adjustment period, the adjustment is made to take place gradually. This is done by integrating in time the dynamical evolution equations, excluding that for PV advection. Instead, the PV anomaly is held fixed in space and ramped up in time from zero to the prescribed PV anomaly at the end of the diagnostic period. Since the PV anomaly is not advected in time, but rather specified, this procedure is in fact an iterative process in which time plays the role of the iteration parameter. It is, however, still useful to measure the length of this iterative process in terms of time.

The diagnostic procedure evolves the horizontal components of the dimensionless horizontal ageostrophic vorticity $\tilde{\boldsymbol{\omega}}_h'$, where we denote $\tilde{\chi} = \chi/f$ for any quantity χ, and where f is the Coriolis frequency (assumed constant). The equation for $\tilde{\boldsymbol{\omega}}_h'$ is obtained from the balance of momentum, mass conservation, and the isochoric condition ($\boldsymbol{\nabla} \cdot \mathbf{u} = 0$); see Dritschel and Viúdez (2003) for details. The result is

$$\frac{\partial \tilde{\boldsymbol{\omega}}_h'}{\partial t} = -\mathbf{u} \cdot \boldsymbol{\nabla} \tilde{\boldsymbol{\omega}}_h' - f\mathbf{k} \times \tilde{\boldsymbol{\omega}}_h' + (1 - c^2)\boldsymbol{\nabla}_h w + \tilde{\boldsymbol{\omega}} \cdot \boldsymbol{\nabla} \mathbf{u}_h + \boldsymbol{\nabla} \mathbf{u}_h \cdot \boldsymbol{\nabla} D, \quad (1)$$

where $\mathbf{u} = (u, v, w)$ and $\mathbf{u}_h$ are the three-dimensional and horizontal velocities, respectively (the subscript $_h$ denotes the horizontal component), $c \equiv N/f$ is the ratio between the mean Brunt–Väisälä frequency and the Coriolis frequency, $\boldsymbol{\omega} = (\xi, \eta, \zeta)$ is the vorticity, $\tilde{\boldsymbol{\omega}}_h' \equiv \tilde{\boldsymbol{\omega}}_h - \boldsymbol{\nabla}_h D$ and $D \equiv c^2 \mathcal{D}$, where $\mathcal{D}$ is the vertical displacement of isopycnals. Both the scaled isopycnal displacement D and scaled velocity $\tilde{\mathbf{u}}$ are calculated from a three-dimensional potential $\boldsymbol{\varphi} = (\varphi, \psi, \phi)$ by $D = -\boldsymbol{\nabla} \cdot \boldsymbol{\varphi}$ and $\tilde{\mathbf{u}} = -\boldsymbol{\nabla} \times \boldsymbol{\varphi}$. The potential $\boldsymbol{\varphi}$ is similar to the one introduced by Muraki et al. [1999, their Eq. (30)]. Once $\tilde{\boldsymbol{\omega}}_h'$ has been advected, the horizontal components of the potential $\boldsymbol{\varphi}_h = (\varphi, \psi)$ are obtained by direct inversion, $\boldsymbol{\varphi}_h = \nabla^{-2}\tilde{\boldsymbol{\omega}}_h'$. The vertical potential ϕ is obtained from the inversion of the "iteration PV anomaly" ϖ_i^g (the prescribed PV anomaly multiplied by a ramp function in time; see below). Since by definition

$$\varpi_i^g = (\tilde{\boldsymbol{\omega}} + \mathbf{k}) \cdot \boldsymbol{\nabla} d - 1 = -\mathcal{D}_z + \tilde{\zeta} - \tilde{\boldsymbol{\omega}} \cdot \boldsymbol{\nabla} \mathcal{D}, \quad (2)$$

where $d(x, y, z, t) = z - \mathcal{D}(x, y, z, t)$ is the isopycnal depth and $(\,)_z \equiv \partial(\,)/\partial z$, we can turn this around into an equation for ϕ,

$$\nabla_h^2 \phi + \epsilon^2 \phi_{zz} - (1 - \epsilon^2)\boldsymbol{\nabla}_h \cdot \boldsymbol{\varphi}_{hz} + \epsilon^2[\nabla^2 \boldsymbol{\varphi} - \boldsymbol{\nabla}(\boldsymbol{\nabla} \cdot \boldsymbol{\varphi})] \cdot \boldsymbol{\nabla}(\boldsymbol{\nabla} \cdot \boldsymbol{\varphi}) - \varpi_i^g = 0, \quad (3)$$

whose inversion (given φ, ψ, and ϖ_i^g; $\epsilon \equiv f/N = c^{-1}$) provides ϕ (see Dritschel and Viúdez 2003).

During the diagnostic period, the iteration PV anom-

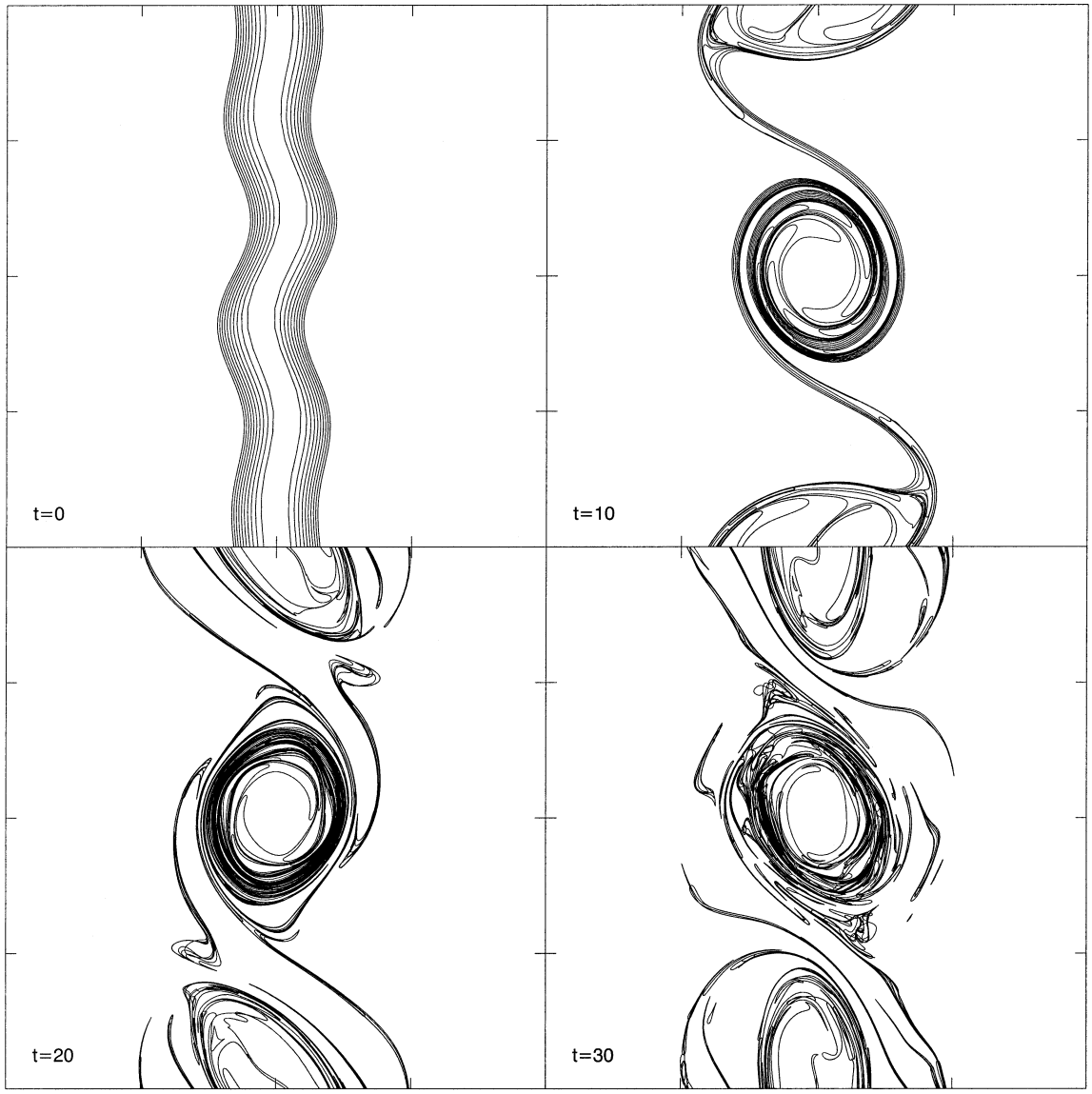

FIG. 1. The PV contours lying on the middle isopycnal surface $l = 33$ ($z = 0$) for the shear zone simulation with minimum PV anomaly $\varpi_m = -0.75$. Times are indicated in inertial periods. There are 10 PV jumps in this layer, each with a magnitude of -0.075.

aly ϖ_i^g is increased smoothly from $\varpi_i^g(\mathbf{x}, t_0) = 0$ at the actual time t_0 to the prescribed geostrophic PV anomaly $\varpi_i^g(\mathbf{x}, t_I) = \varpi_0^g(\mathbf{x})$ at the end of the diagnostic time $t_I = t_0 + \Delta t_I$, where Δt_I is the diagnostic time interval, using a ramp function $W(t)$,

$$\varpi_i^g(\mathbf{x}, t) \equiv \varpi_0^g(\mathbf{x})W(t),$$

$$W(t) \equiv \frac{1}{2}\left\{1 - \cos\left[\frac{\pi(t - t_0)}{\Delta t_I}\right]\right\}, \qquad t_0 \le t \le t_I. \tag{4}$$

Thus, during the diagnostic period the diagnostic velocity and density fields grow smoothly from zero in response to the slow growth of ϖ_i^g. The field $\varpi_0^g(\mathbf{x})$ is the prescribed dimensionless geostrophic PV anomaly

$$\varpi_0^g \equiv (\tilde{\boldsymbol{\omega}}_0^g + \mathbf{k}) \cdot \boldsymbol{\nabla} d_0 - 1 = -\mathcal{D}_{0z} + \tilde{\zeta}_0^g - \tilde{\boldsymbol{\omega}}_0^g \cdot \nabla \mathcal{D}_0,$$

where the subscript zero means the actual value and the superscript g means the corresponding geostrophic quantity. Thus $\varpi_0^g(\mathbf{x})$ is obtained from the actual, assumed known, density field. Note that W is smooth at $t = t_0$ and at $t = t_I$ [$W(t_0) = 0$, $W(t_I) = 1$, $W_t(t_0) = W_t(t_I) = 0$, where $(\,)_t \equiv \partial(\,)/\partial t$]. This smoothness helps to minimize the initial generation of IGWs.

3. Applications

a. Numerical parameters

We consider a three-dimensional periodic domain having $(n_X, n_Y, n_Z) = (64, 64, 64)$ grid points, an equal

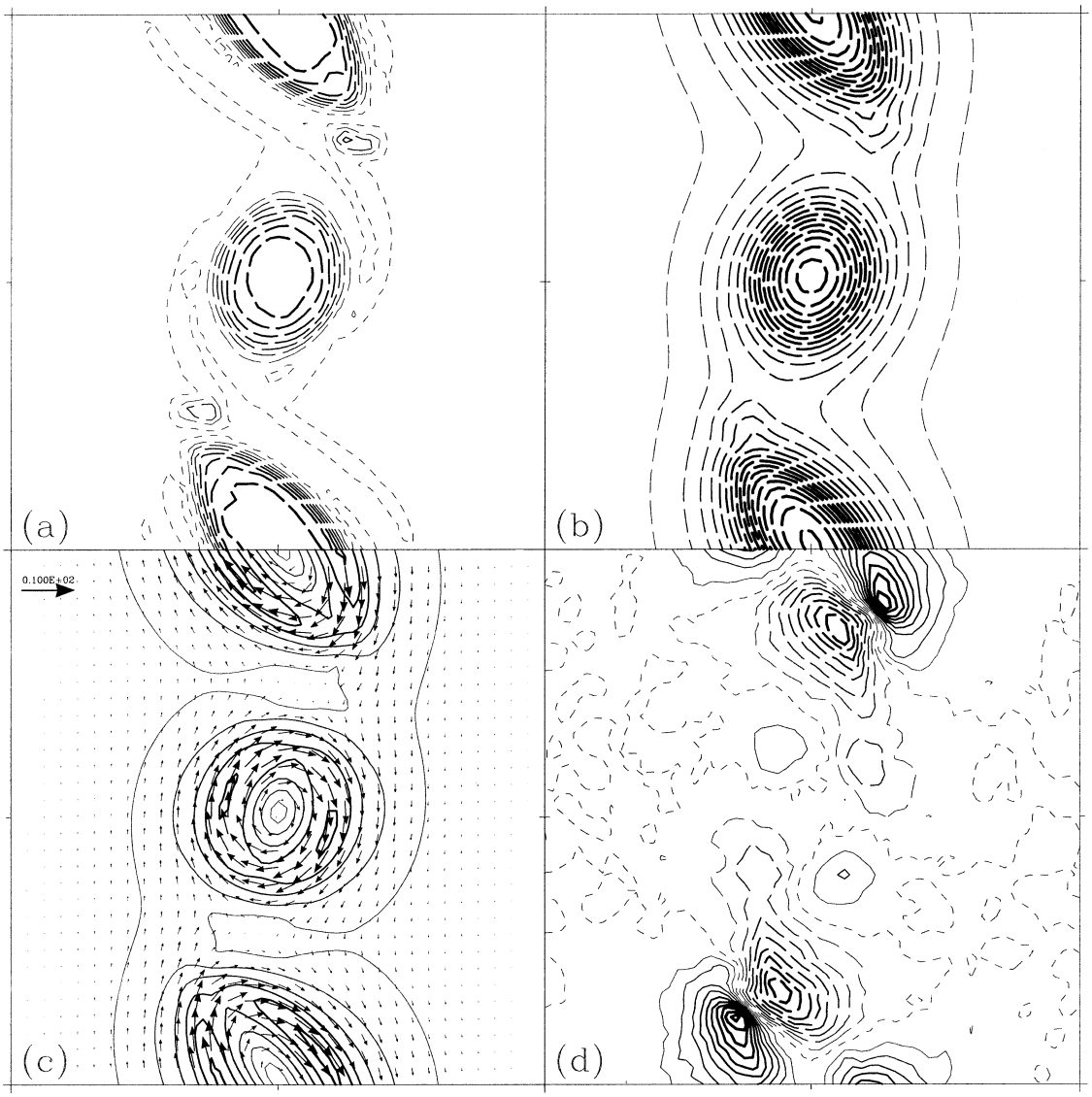

FIG. 2. Horizontal distributions of (a) PV anomaly ϖ_0 ($\times 10$, $i_Z = 33$), (b) vertical displacement $\mathcal{D}_0$ ($\times 10^2$, $i_Z = 28$), (c) horizontal velocity $\mathbf{u}_{h0}$ ($\times 5$, $i_Z = 33$; for clarity only every other vector is plotted), and (d) vertical velocity w_0 ($\times 4 \times 10^4$, $i_Z = 28$). Contour interval $\Delta = 1$ in this and subsequent contour plots.

number of isopycnal surfaces n_l, a vertical extension $L_Z = 2\pi$ (in arbitrary space units), and horizontal extensions L_X and L_Y prescribed by the ratios $L_X/L_Z = L_Y/L_Z = 100$. This ratio is equal to the ratio of the mean Brunt–Väisälä to Coriolis frequency $c \equiv N/f = 100$, where $N = 2\pi$ (in arbitrary time units). Thus the time interval of one (mean) buoyancy period is $\Delta t = 1$. One inertial period (i.p.) equals 100 buoyancy periods. The time step is set to $\delta t = 0.1$ (a tenth of a buoyancy period). A biharmonic hyperdiffusion term, producing a small damping rate (*e* folding) of $e_f = 10$ per *inertial period* at the highest wavenumber, is added to the equations for the rate of change of the horizontal ageostrophic vorticity. Two simulations were carried out until $t = 30$ i.p.; however, we chose a diagnostic or ''actual'' time $t_0 = 20$ i.p. Note that t_0 is well beyond the end of the initialization period of these simulations (which occurs over the first 5 i.p.); this period is also taken to be the diagnostic time interval, that is, $\Delta t_I = 5$ i.p. This is long enough to keep IGWs of secondary importance (Viúdez and Dritschel 2003; Dritschel and Viúdez 2003).

It is noteworthy that the characteristics of the numerical model used are independent of the PVI technique. The numerical model, which explicitly conserves PV through the advection of PV contours, is only used to provide dynamically consistent velocity and density fields at $t = t_0$. The diagnosis of ageostrophic motion through dynamic PVI makes no use of the PV contour dynamics since the target PV field $\varpi_0^g(\mathbf{x})$ is fixed in time.

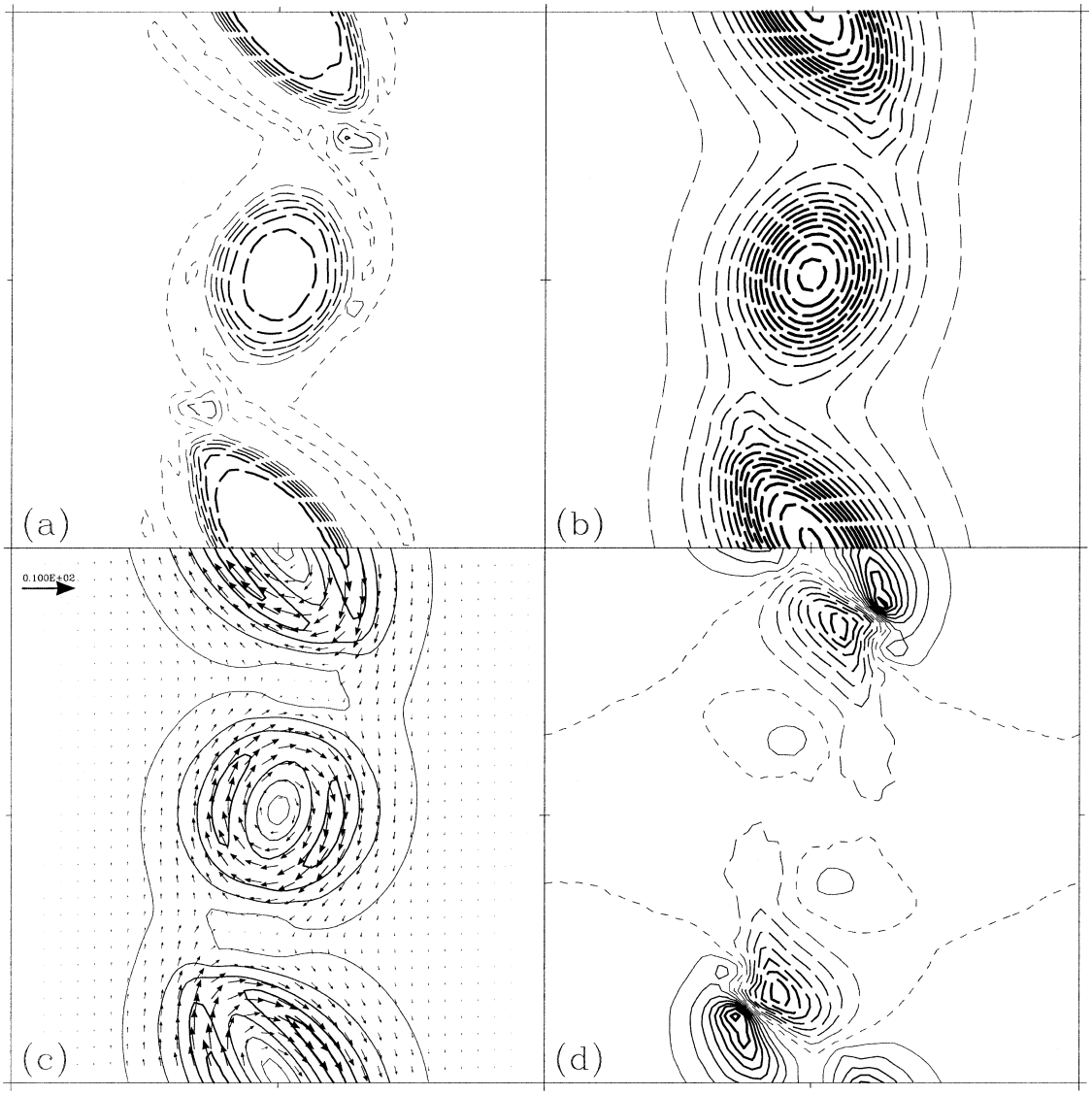

FIG. 3. As in Fig. 2 but for the diagnosed fields: (a) the geostrophic PV anomaly $\hat{\varpi} = \varpi_0^g$, (b) $\hat{\mathcal{D}}$, (c) $\hat{\mathbf{u}}_h$, and (d) $\hat{w}$.

Inherent to the PVI approach is the inversion of the geostrophic PV field. Whether this PV inversion is made in terms of potentials, as is done here, or in terms of other diagnostic quantities is an independent matter. Well-posed boundary conditions for these diagnostic quantities in the PV inversion are, with the exception of the triply periodic domain used here, always required. Zero normal velocity boundary conditions may be implemented using the Fourier sine or cosine spectral modes instead of the full Fourier transform for the potentials. Specification of more general boundary conditions arising, for instance, in realistic ocean environments, is not essential for the present purposes.

b. A shear zone

In this first simulation the initial PV anomaly is confined to a circular horizontal cylinder (after stretching the height coordinate by c) with radius $r_e = 0.5c$ (the basic PV) plus a horizontal transverse PV disturbance (as in Dritschel and Viúdez 2003). The basic undisturbed flow is steady, with fluid moving in the y direction only. The initial PV contours (before model initialization, at $t = 0$) lie on flat isopycnal surfaces ($\mathcal{D} = 0$), and are chosen to represent the circular distribution of ϖ in the yz plane, $\varpi(r) = \varpi_m(1 - r^2/r_e^2)$, where ϖ_m is the maximum PV anomaly and here $r^2 = [x - x_d(y)]^2 + z^2$, where $x_d(y)$ is the centreline displacement used to impart a disturbance to the cylinder. We take $x_d(y) = a_1 \sin(2\pi m_1 y/L_Y) + a_2 \sin(2\pi m_2 y/L_Y)$, with $m_1 = 2$, $m_2 = 3$, $a_1 = 0.1$, and $a_2 = -0.1$ (see Fig. 1). Full details may be found in Dritschel and Viúdez (2003). Here we choose a large PV anomaly $\varpi_m = -0.75$ to verify that the PVI works satisfactorily for highly ageostrophic flows, which are in principle capable of signif-

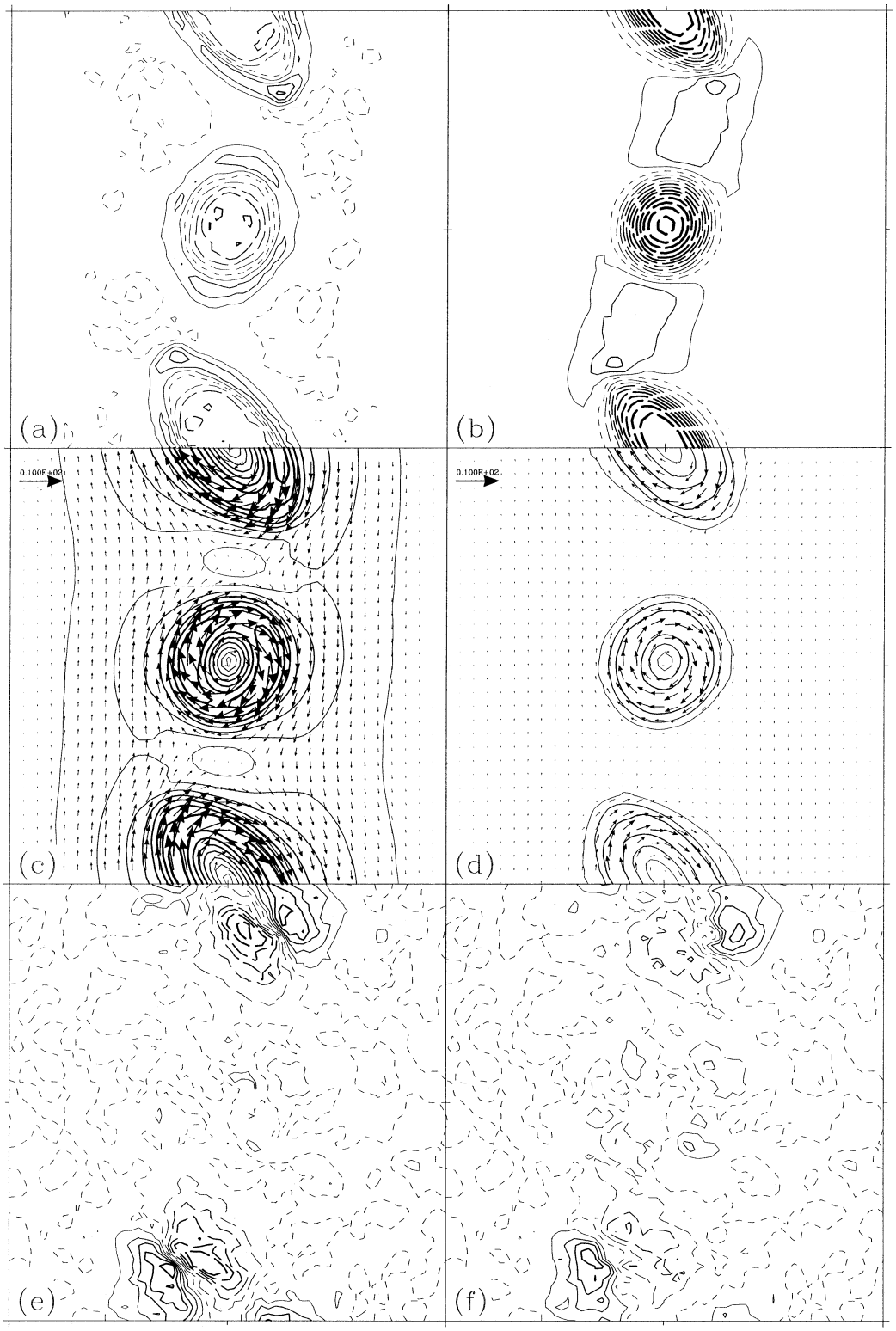

FIG. 4. Horizontal distributions of (a) PV difference $\varpi_0 - \varpi_0^q$ ($\times 40$, $i_Z = 33$), (b) vertical displacement difference $\mathcal{D}_0 - \hat{\mathcal{D}}$ ($\times 10^3$, $i_Z = 28$), (c) ageostrophic horizontal velocity $\mathbf{u}_{h0} - \mathbf{u}_{h0}^q$ ($\times 20$, $i_Z = 33$), (d) horizontal velocity difference $\mathbf{u}_{h0} - \hat{\mathbf{u}}_h$ ($\times 20$, $i_Z = 33$), (e) $w_0 - w_0^q$ ($\times 8 \times 10^4$, $i_Z = 28$), and (f) $w_0 - \hat{w}$ ($\times 8 \times 10^4$, $i_Z = 28$).

TABLE 1. Statistics (maximum and rms values) for the shear and jet simulations at $t = 20$ i.p. The ratio refers to the ratio between the rms values. For the comparison of the vertical velocity fields we have used a threshold value $w_0 = 0.5 \times 10^{-4}$.

Case	Max $\lvert\mathbf{u}_{h0}\rvert$	Max $\lvert w_0\rvert$ ($\times 10^{-4}$)	Rms $\mathbf{u}_{h0} - \mathbf{u}^q_{h0}$ ($\times 10^{-2}$)	Rms $\mathbf{u}_{h0} - \hat{\mathbf{u}}_h$ ($\times 10^{-2}$)	Ratio	Rms $w_o - w_0^q$ ($\times 10^{-5}$)	Rms $w_0 - \hat{w}$ ($\times 10^{-5}$)	Ratio
Shear	1.24	3.04	10.8	2.94	3.67	3.54	2.31	1.53
Jet	1.76	3.85	14.9	4.20	3.55	2.71	2.35	1.15

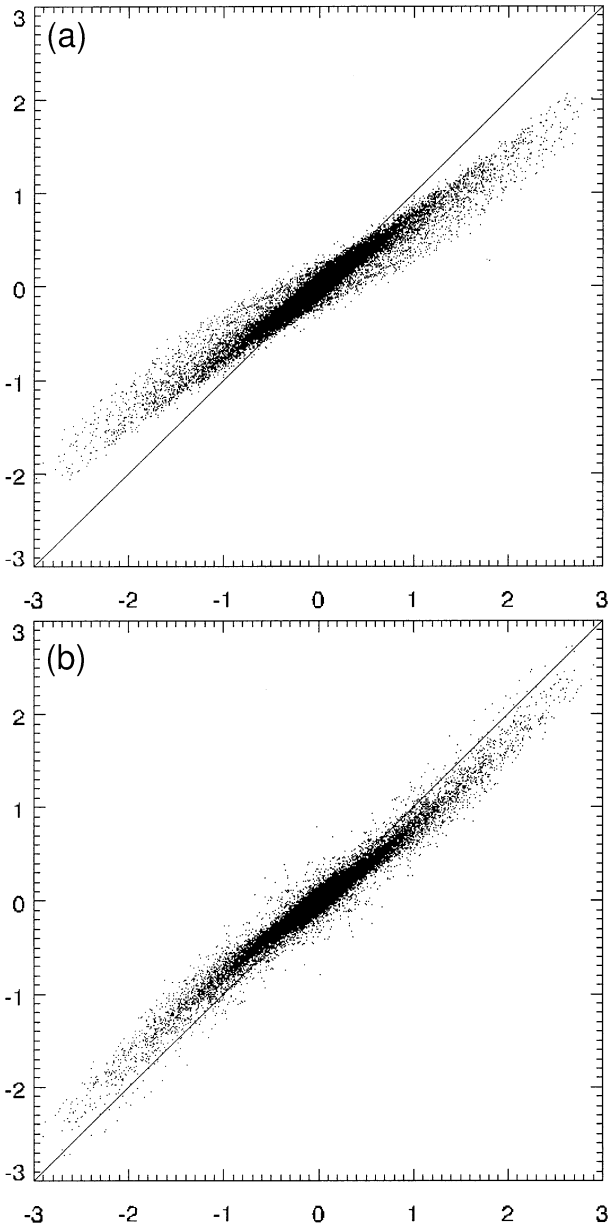

FIG. 5. Scatterplot of (a) the QG vertical velocity w_0^q (vertical axis) and (b) the diagnosed vertical velocity $\hat{w}$ (vertical axis) vs the total vertical velocity w_0 (horizontal axis) for the shear zone (in units of 10^{-4}).

icant spontaneous generation of IGWs. The maximum Rossby number of this simulation is $|\min(\tilde{\zeta})| = 0.62$, comparable to $|\varpi_m|$, and the maximum Froude number, $\max(F_r) = 0.36$. The Froude number is here defined as $F_r \equiv \omega_h/\mathcal{N}$, the ratio between the magnitude of the horizontal vorticity $\omega_h \equiv |\boldsymbol{\omega}_h|$ and the total Brunt–Väisälä frequency $\mathcal{N} \equiv (-g\rho_z/\rho_0)^{1/2} = N(1 - \epsilon^2 D_z)^{1/2}$.

This negative PV anomaly distribution corresponds to a three-dimensional shear current whose evolution is shown in Fig. 1. During the initial stages of the instability, the PV cylinder rolls up into a street of stable anticyclonic vortices with the same PV anomaly in their cores ($\varpi = -0.75$) but with different eccentricities. At $t = t_0$, the vortices induce a negative isopycnal displacement $\mathcal{D}_0$ (Fig. 2b) with $\min(\mathcal{D}_0) = -0.17$ in the more eccentric vortex's center at the depth of maximum vertical velocity (vertical grid point $i_Z = 18$ or depth $z = -1.47$). At the midplane ($i_Z = 33$, $z = 0$), $\mathbf{u}_{h0}$ has maximum values of $\max(|\mathbf{u}_{h0}|) \sim 1.2$ and 1.0 along both sides of the eccentric and circular vortex, respectively (Fig. 2c), while w_0 (Fig. 2d) shows a quadrupole distribution for both vortices with maximum values

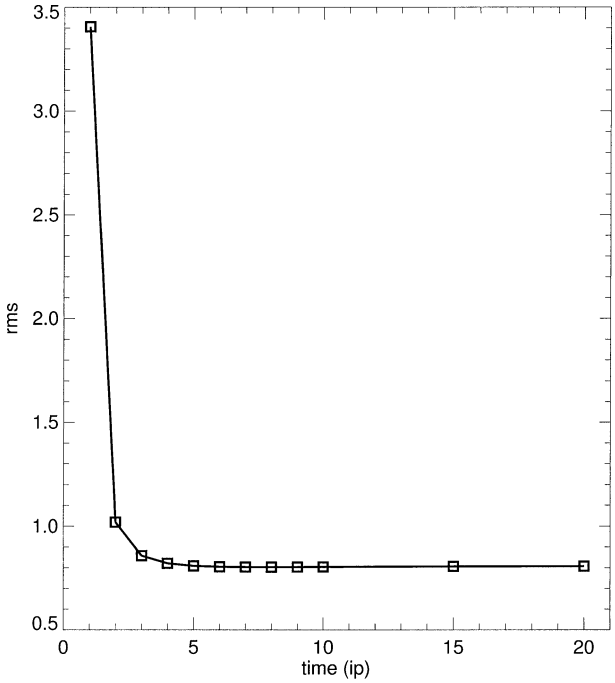

FIG. 6. The rms of $w_0^q - \hat{w}_{\Delta t_I}$ ($\times 10^8$ and $t = 20$ i.p.) over the entire domain as a function of the time interval Δt_I (in inertial periods).

$\max(|w_0|) \sim 2.3 \times 10^{-4}$ around the eccentric vortex. The quadrupole distribution of w_0 can be inferred from the horizontal distributions of PV (Fig. 1c) and $\mathcal{D}_0$ (Figs. 2a,b); see Viúdez and Dritschel (2003) for details.

The displacement field $\mathcal{D}_0$ [at time $t_0 = 20$ i.p., when $\min(\tilde{\zeta}_0) = -0.58$] is used to carry out the PVI diagnosis from the geostrophic PV anomaly ϖ_0^g. This field ϖ_0^g (Fig. 3a) closely resembles the total field ϖ_0 (Fig. 2a) though, as expected, $|\varpi_0^g|$ is smaller than $|\varpi_0|$. The maximum differences between both fields (Fig. 4a) are about $\max(|\varpi_0 - \varpi_0^g|) = 0.075$, or one-tenth of $\max(|\varpi_0|)$. Because of this small difference, the diagnosed displacement $\hat{\mathcal{D}}$ [Fig. 3b, with $\max(|\hat{\mathcal{D}}|) \sim 0.16$] also shows small differences from $\mathcal{D}_0$, with $\max(|\mathcal{D}_0 - \hat{\mathcal{D}}|) \sim 1.0 \times 10^{-2}$ (Fig. 4b).

The diagnosed horizontal velocity $\hat{\mathbf{u}}_h$ (Fig. 3c) shows the same pattern as $\mathbf{u}_{h0}$ with maxima also along the narrow sides of the vortices. However, $\max(|\hat{\mathbf{u}}_h|) \sim 1.0$ at $z = 0$, and this is clearly smaller than $|\mathbf{u}_{h0}|$ (Fig. 2c). Nevertheless, for these highly ageostrophic vortices, $\hat{\mathbf{u}}_h$ better approximates $\mathbf{u}_h$ than does the geostrophic velocity $\mathbf{u}_{h0}^g$. The differences $\mathbf{u}_{h0} - \mathbf{u}_{h0}^g$ (Fig. 4c) and $\mathbf{u}_{h0} - \hat{\mathbf{u}}_h$ (Fig. 4d) show that $\max(|\mathbf{u}_{h0} - \mathbf{u}_{h0}^g|) \sim 0.40$ while $\max(|\mathbf{u}_{h0} - \hat{\mathbf{u}}_h|) \sim 0.15$. A large part of the geostrophic imbalance $|\mathbf{u}_{h0} - \mathbf{u}_{h0}^g|$ is due to missing the horizontal advective acceleration $\mathbf{u}_{h0} \cdot \nabla \mathbf{u}_{h0}$. The gradient balance (balance between the horizontal advective and Coriolis accelerations with the pressure gradient term) is usually more accurate than geostrophic balance in mesoscale dynamics with large Rossby numbers (Viúdez et al. 2000; Shearman et al. 2000). The statistics (see Table 1) indicate that the root-mean-square (rms) of $\mathbf{u}_{h0} - \hat{\mathbf{u}}_h$ is about one-third that of $\mathbf{u}_{h0} - \mathbf{u}_{h0}^g$.

The diagnosed vertical velocity $\hat{w}$ (Fig. 3d) displays the same quadrupole pattern in every vortex as w_0 (Fig. 2d), but $\hat{w}$ is virtually free of IGWs, and its magnitude [$\max(|\hat{w}|) \sim 2.0 \times 10^{-4}$] is smaller than $|w_0|$ [$\max(|w_0|) \sim 2.3 \times 10^{-4}$]. In this respect $\hat{w}$ is similar to the QG vertical velocity w_0^q. The difference $w_0 - w_0^q$ (Fig. 4e), where w_0^q is obtained here solving the QG omega equation, has $\max(|w_0 - w_0^q|) \sim 0.75 \times 10^{-4}$, while the difference $w_0 - \hat{w}$ (Fig. 4f) has $\max(|w_0 - \hat{w}|) \sim 0.50 \times 10^{-4}$. The statistical values (see Table 1) indicate that the rms of $w_0 - \hat{w}$ is about 0.65 times that of $w_0 - w_0^q$.

The differences between w_0^q and $\hat{w}$ may be better appreciated in the scatterplots of w_0^q and $\hat{w}$ versus w_0 (Figs. 5a,b). The amount of scatter is interpreted principally as IGW activity, though part of this scatter is also due to small-scale differences between the balanced vortical parts of the QG, PVI, and total flows. The slope of the linear regressions is hence interpreted as the difference between QG- and PVI-diagnosed balance. The amount of scatter is quantified here as the average of the distances, in velocity space, of the points $\{w_0(\mathbf{x}), \hat{w}_0(\mathbf{x})\}$, and $\{w_0(\mathbf{x}), w_0^q(\mathbf{x})\}$, to the corresponding regression line. Statistical values are computed using magnitudes of w_0, w_0^q, and $\hat{w}$ larger than 0.5×10^{-4}. The scatter

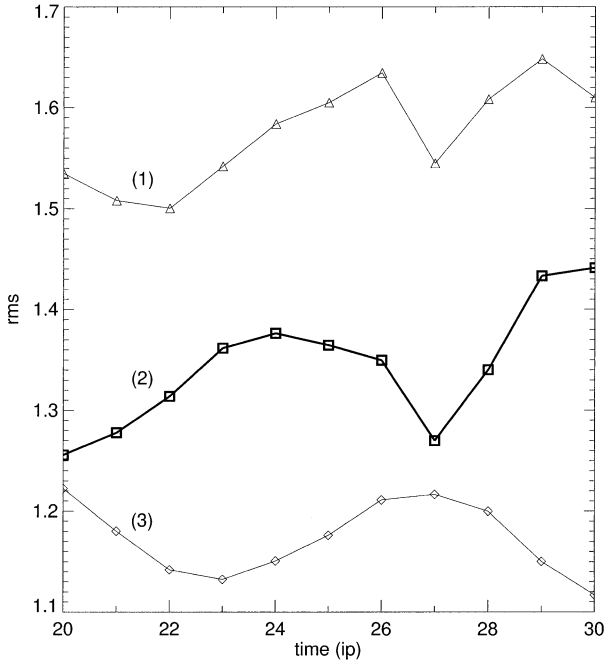

FIG. 7. Time series of the rms of $w_0^q - w_0$ [$\times 10^8$, (1)] and $\hat{w}_0 - w_0$ [$\times 10^8$, (2)] from $t_0 = 20$ to $t_0 = 30$ i.p. The third line (3) shows the ratio between the above rms values $\text{rms}(w_0^q - w_0)/\text{rms}(\hat{w}_0 - w_0)$. Diagnostic time interval $\Delta t_I = 5$ i.p.

of $\hat{w}$ with respect to w_0 is 6.6×10^{-6}, smaller than that of w_0^q (7.6×10^{-6}). This indicates again that IGW activity is lower in the PVI diagnosis. The linear regressions $w_0^q(\mathbf{x}) = s^q w_0(\mathbf{x})$ and $\hat{w}(\mathbf{x}) = \hat{s} w_0(\mathbf{x})$ give slopes $s^q = 0.60$ and $\hat{s} = 0.86$. Thus, we conclude that $\hat{\mathbf{u}}_h$ and $\hat{w}$ better approximate $\mathbf{u}_{h0}$ and w_0 than do the geostrophic $\mathbf{u}_{h0}^g$ and the QG w_0^q.

Various numerical integrations using *different* diagnostic time intervals Δt_I show that, in terms of the rms difference $w_0^q - \hat{w}_{\Delta t_I}$, where $\hat{w}_{\Delta t_I}$ is the PVI diagnosed vertical velocity using a time interval Δt_I, convergence is reached for $\Delta t_I \geq 4$ inertial periods (Fig. 6).

The improvement of $\hat{w}$ over w^q is a robust result, characteristic of the whole numerical simulation, and is independent on the specific diagnostic time t_0. The time series of the rms of $\hat{w}_0 - w_0$ and $w_0^q - w_0$ for diagnostic times $t_0 = 20, \ldots, 30$ i.p. (Fig. 7) show that the rms of $\hat{w}_0 - w_0$ is always smaller than that of $w_0^q - w_0$, the average ratio $\text{rms}(w_0^q - w_0)/\text{rms}(\hat{w}_0 - w_0) \approx 1.17$.

c. An oceanic jet

As a second example we analyze a model oceanic flow containing both positive and negative PV anomalies. A jet current is set up by placing two horizontal PV cylinders of opposite sign next to each other (Fig. 8). This PV distribution induces a fast northward current with two slower southward currents running along the flanks of the two-cylinder system. Each cylinder has a horizontal dimension of $0.5c$ as before, but a larger ver-

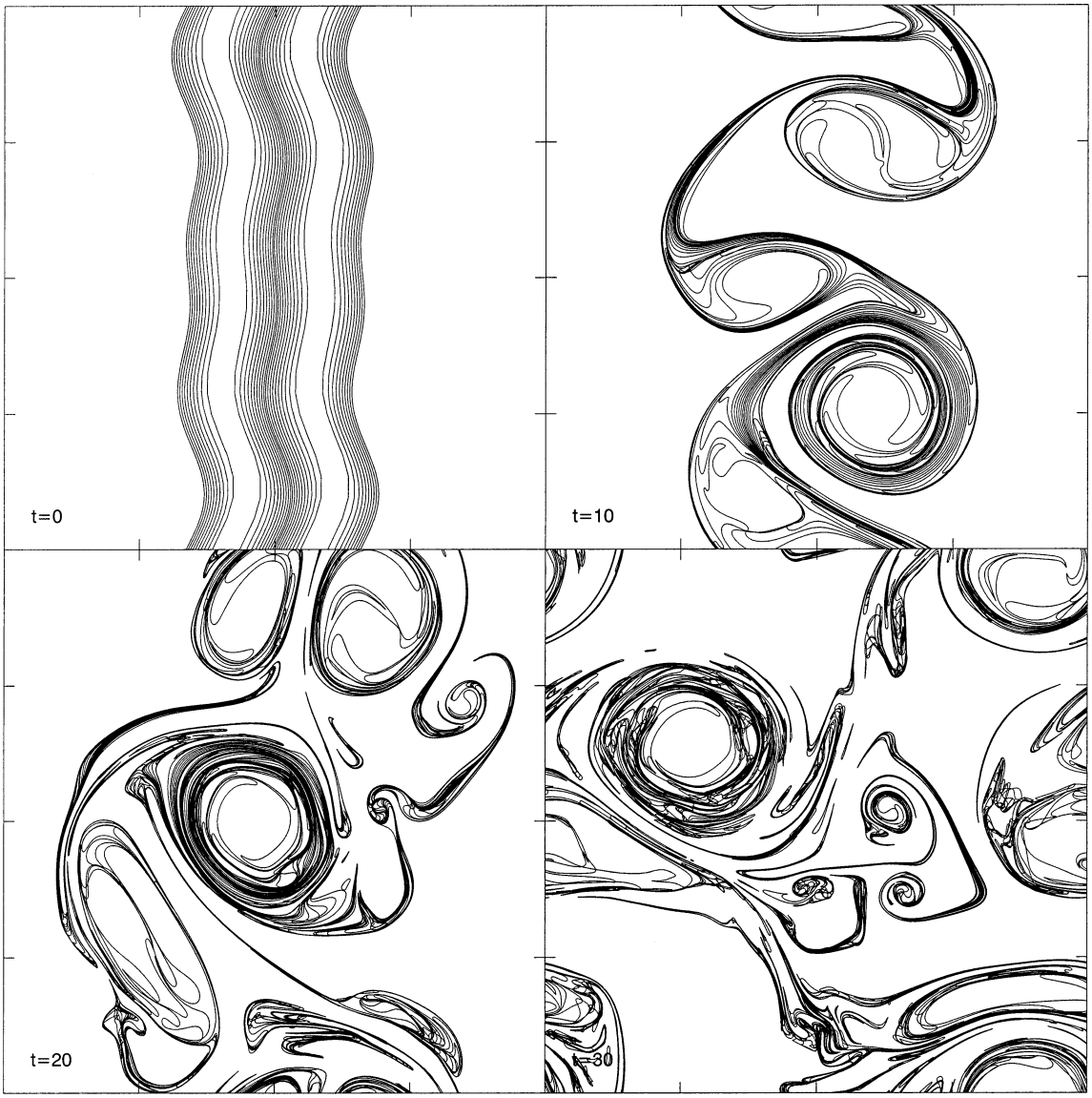

FIG. 8. Time evolution of the PV contours lying on the middle isopycnal surface $l = 33$ for the jet with maximum PV anomaly $|\varpi_m| = 0.75$. Times are indicated in inertial periods (from $t = 10$ to $t = 30$ i.p.). There are 20 PV jumps in this layer, each with a magnitude of 0.075.

tical dimension of $1/\sqrt{2}$ so that the two cylinders touch each other at the origin and just fit within a circle of radius $0.5c$ [after stretching the height coordinate by c; again see Dritschel and Viúdez (2003) for details]. We take the maximum and minimum PV anomalies to be $\varpi_m = \pm 0.75$, which leads to a maximum Rossby number $\max(\tilde{\zeta}) = 0.80$ and maximum Froude number $\max(\mathrm{F_r}) = 0.42$. As the flow evolves, the PV rolls up into a street of large cyclonic and anticyclonic vortices that pair, forming mushroom-like eddy structures, from which small-scale eddies are later detached. This flow is notably more complex and ageostrophic than the previous one considered (cf. Fig. 1).

The cyclonic and anticyclonic vortices have positive and negative isopycnal vertical displacements $\mathcal{D}_0$, respectively, (Fig. 9b) with $\max(|\mathcal{D}_0|) = 0.14$ in the northern anticyclonic vortex's center at the depth of maximum vertical velocities ($i_z = 28$, $z = -0.49$). At the middle layer ($i_z = 33$, $z = 0$) $\mathbf{u}_{h0}$ is greatest between each vortex pair, with $\max(|\mathbf{u}_{h0}|) \sim 1.6$ in the northern pair (Fig. 9c), while w_0 (Fig. 9d) has again a quadrupole distribution associated in this case with each vortex pair, and has a maximum value of $\max(|w_0|) \sim 3 \times 10^{-4}$ around the northern pair.

The displacement field $\mathcal{D}_0$ [at time $t_0 = 20$ i.p., when $\min(\tilde{\zeta}) = -0.67$], is next used to carry out the PVI diagnosis. From $\mathcal{D}_0$ we compute the geostrophic PV anomaly ϖ_0^g (Fig. 10a), which again closely resembles

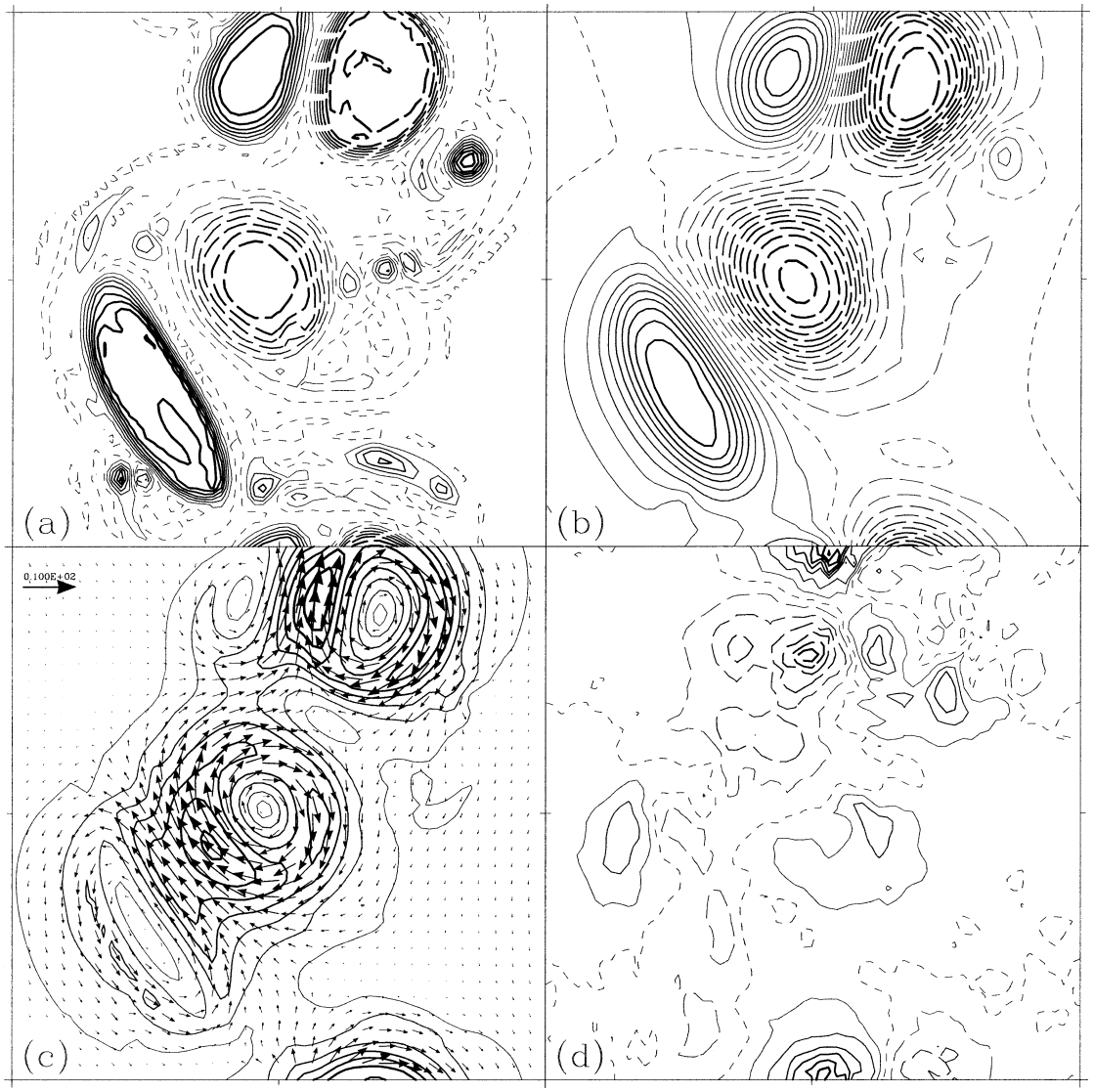

FIG. 9. Horizontal distributions of (a) PV anomaly ϖ_0 ($\times 10$, $i_z = 33$), (b) vertical displacement $\mathcal{D}_0$ ($\times 10^2$, $i_z = 28$), (c) horizontal velocity $\mathbf{u}_{h0}$ ($\times 5$, $i_z = 33$; only every other vector is plotted), and (d) vertical velocity w_0 ($\times 2 \times 10^4$, $i_z = 28$).

the total ϖ_0 (Fig. 9a), but with $|\varpi_0^g|$ slightly smaller than $|\varpi_0|$. The maximum difference between these fields (Fig. 11a) is $\max(|\varpi_0 - \varpi_0^g|) \sim 0.15$, or one-tenth of the maximum PV anomaly difference [$\max(\varpi_0) - \min(\varpi_0) = 2\varpi_m = 1.5$]. The diagnosed displacement $\hat{\mathcal{D}}$ [Fig. 10b, with $\max(|\hat{\mathcal{D}}|) \sim 0.13$] also shows small differences from $\mathcal{D}_0$, with $\max(|\mathcal{D}_0 - \hat{\mathcal{D}}|) \sim 1.2 \times 10^{-2}$ (Fig. 11b).

The diagnosed horizontal velocity $\hat{\mathbf{u}}_h$ (Fig. 10c) shows the same pattern as $\mathbf{u}_{h0}$ with maxima at the junction of each pair of vortices and having $\max(|\hat{\mathbf{u}}_h|) \sim 1.4$ at the midplane $z = 0$. It is again clearly smaller than $|\mathbf{u}_{h0}|$ (Fig. 9c); however, the diagnosed $\hat{\mathbf{u}}_h$ is still a better approximation than the geostrophic velocity $\mathbf{u}_{h0}^g$. The differences $\mathbf{u}_{h0} - \mathbf{u}_{h0}^g$ (Fig. 11c) and $\mathbf{u}_{h0} - \hat{\mathbf{u}}_h$ (Fig. 11d) show that $\max(|\mathbf{u}_{h0} - \mathbf{u}_{h0}^g|) \sim 0.60$ while $\max(|\mathbf{u}_{h0} - \hat{\mathbf{u}}_h|) \sim 0.30$. The rms of $\mathbf{u}_{h0} - \hat{\mathbf{u}}_h$ (Table 1) is again about one-third of the rms of $\mathbf{u}_{h0} - \mathbf{u}_{h0}^g$. In this case the largest ageostrophic motion is located at the junction of the vortices, being strongest along the periphery of the anticyclones.

The diagnosed vertical velocity $\hat{w}$ (Fig. 10d) has a similar distribution to w_0 (Fig. 9d) but essentially without IGWs. Its maximum magnitude [$\max(|\hat{w}|) \sim 3.0 \times 10^{-4}$] is nearly identical to that of $|w_0|$ [$\max(|w_0|) \sim 3.0 \times 10^{-4}$]. The diagnosed $\hat{w}$ is again similar to the QG vertical velocity w_0^q. The differences $w_0 - w_0^q$ [Fig. 11e, with $\max(|w_0 - w_0^q|) \sim 1.5 \times 10^{-4}$] and $w_0 - \hat{w}$ (Fig. 11f) [with $\max(|w_0 - \hat{w}|) \sim 1.5 \times 10^{-4}$] both show the presence of IGWs. However, the scatter for w_0^q versus w_0 (Fig. 12a) is 1.3×10^{-5}, larger than the scatter for $\hat{w}$ versus w_0 (Fig. 12b), which is 1.0×10^{-5}.

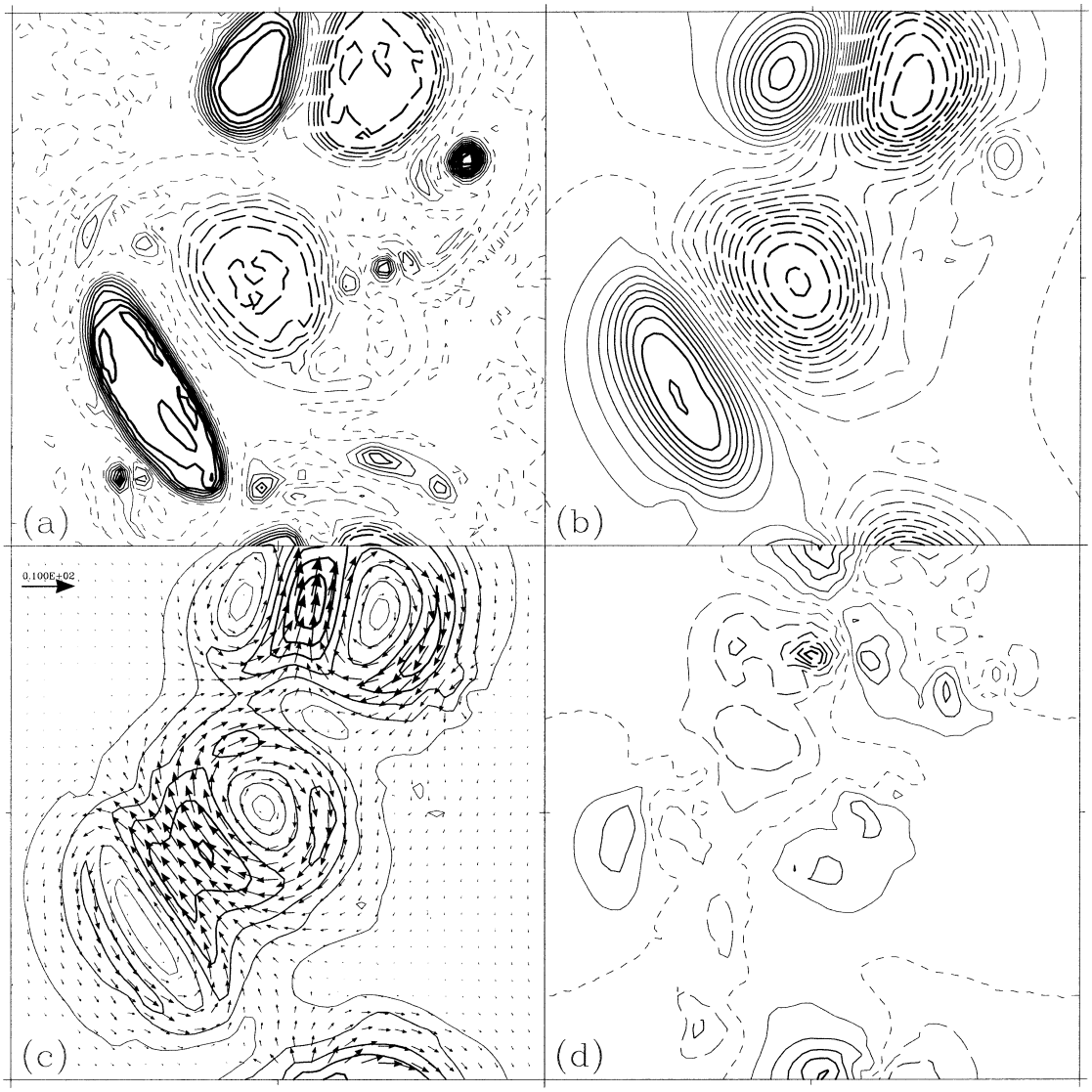

FIG. 10. As in Fig. 9 but for the diagnosed fields: (a) the geostrophic PV anomaly $\hat{\varpi} = \varpi_0^g$, (b) $\hat{\mathcal{D}}$, (c) $\hat{\mathbf{u}}_h$, and (d) $\hat{w}$.

Both values are larger than the scatter in the shear current case.

We note that in flows with only negative PV anomalies (as in the shear current example above) $|w_0^q|$ is smaller than $|w_0|$, while usually the opposite occurs in flows with only positive PV anomalies (Viúdez and Dritschel 2004). In flows having both positive and negative PV anomalies (as in this case) the slope in the linear regression w_0^q versus w_0 would be closer to 1 than that in flows with single-valued PV anomalies only because of the average between two slopes, larger and smaller than 1, and therefore it would not be a good indication of the departure of the QG- and PVI-diagnosed vertical velocity from the slow ''balanced'' solution.

In terms of spatially averaged absolute differences, we find $\langle |w_0 - \hat{w}| \rangle = 6.6 \times 10^{-6}$ while $\langle |w_0 - w_0^q| \rangle = 6.8 \times 10^{-6}$.The rms of $w_0 - \hat{w}$ (Table 1) is about 0.87 times the rms of $w_0 - w_0^q$. Thus, as in the previous example, we conclude that $\hat{\mathbf{u}}_h$ and $\hat{w}$ better approximate $\mathbf{u}_{h0}$ and w_0 than do the geostrophic $\mathbf{u}_{h0}^g$ and the QG w_0^q.

4. Concluding remarks

In this work we have introduced a new method, based on the dynamic initialization of potential vorticity, for diagnosing the approximately balanced three-dimensional velocity from a given density field in the ocean. Applications of the method to simulated oceanic flows confirmed that it is able to diagnose balanced horizontal and vertical velocity fields that improve the estimates given by the geostrophic and quasigeostrophic approximations.

We are currently exploring the use of PVI as an ini-

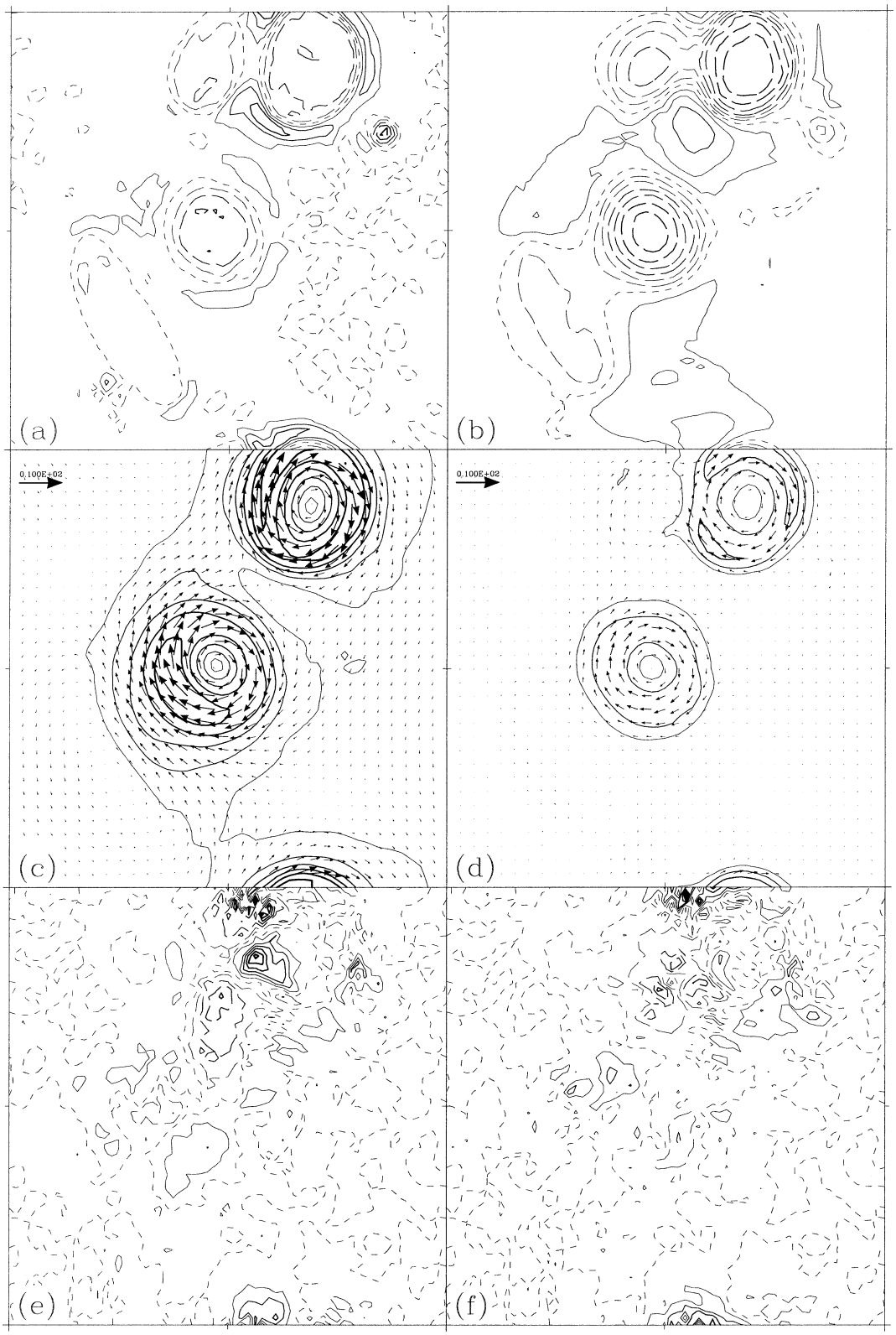

FIG. 11. Horizontal distributions of (a) PV difference $\varpi_0 - \varpi_0^g$ ($\times 20$, $i_Z = 33$), (b) vertical displacement difference $\mathcal{D}_0 - \hat{\mathcal{D}}$ ($\times 5 \times 10^2$, $i_Z = 28$), (c) ageostrophic horizontal velocity $\mathbf{u}_{h0} - \mathbf{u}_{h0}^g$ ($\times 10$), (d) horizontal velocity difference $\mathbf{u}_{h0} - \hat{\mathbf{u}}_h$ ($\times 10$), (e) $w_0 - w_0^q$ ($\times 4 \times 10^4$, $i_Z = 28$), and (f) $w_0 - \hat{w}$ ($\times 4 \times 10^4$, $i_Z = 28$).

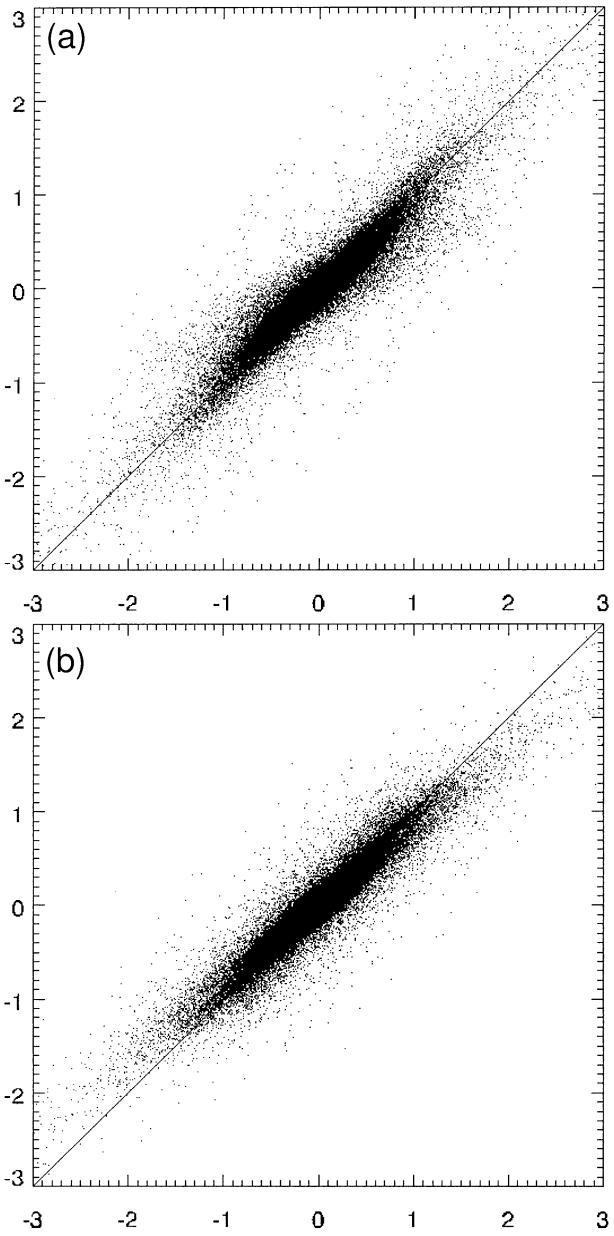

FIG. 12. Scatterplot of (a) the QG vertical velocity w_0^q (vertical axis) and (b) the diagnosed vertical velocity $\hat{w}$ (vertical axis) vs the total vertical velocity w_0 (horizontal axis) for the oceanic jet (in units of 10^{-4}).

tialization method, to provide balanced fields from a given, exactly known potential vorticity field. The results of the present paper show that PVI may be promising in this respect also. A test experiment using the PVI method but replacing the geostrophic PV with the the actual PV as the target PV provided a horizontal velocity field closer to the actual horizontal velocity than the PVI-diagnosed one, but the resulting vertical velocity was in fact worse than the one diagnosed by PVI using the geostrophic PV. This might be a consequence of the artificial nonadvection of the PV contours during the PVI period. Using the total PV leads to an increase of the maximum magnitude of both the PVI-diagnosed horizontal velocity and isopycnal displacement. Since the PV field is not advected, the phase velocity of otherwise rotating elliptical eddies, as well as the propagation speed of otherwise moving dipoles, is zero. This implies that, since density is still exactly conserved, fluid particles move with larger horizontal speeds on more sloped steady isopycnals. Thus, balanced vertical velocities are overestimated using the PVI method. We are currently investigating an alternative approach that may overcome this difficulty. This approach starts directly from the PV and obtains the other fields, such as density and velocity, by the same time integration technique lying at the heart of the PVI method. This may help one to more clearly distinguish balanced (vortical) and imbalanced (wave) fields.

Acknowledgments. Support for this research has come from the Spanish Ministerio de Ciencia y Tecnología Grant REN2002-01343 and the program Ramón y Cajal 2001, as well as the U.K. National Environment Research Council (Grant GR3/11899). Comments from two reviewers are very much appreciated.

REFERENCES

Allen, J. S., 1993: Iterated geostrophic intermediate models. *J. Phys. Oceanogr.,* **23,** 2447–2461.

Daley, R., 1991: *Atmospheric Data Analysis.* Cambridge University Press, 457 pp.

Dritschel, D. G., and A. Viúdez, 2003: A balanced approach to modelling rotating stably-stratified geophysical flows. *J. Fluid Mech.,* **488,** 123–150.

Eliassen, A., 1948: The quasi-static equations of motion. *Geofys. Publ.,* **17** (3), 1–44.

Gent, P. R., and J. C. McWilliams, 1983: Consistent balance models in bounded and periodic domains. *Dyn. Atmos. Oceans,* **7,** 67–93.

Hoskins, B. J., 1975: The geostrophic momentum approximation and the semi-geostrophic equations. *J. Atmos. Sci.,* **32,** 233–242.

Lynch, P., and X.-Y. Huang, 1992: Initialization of the HIRLAM model using a digital filter. *Mon. Wea. Rev.,* **120,** 1019–1034.

Muraki, D. J., C. Snyder, and R. Rotunno, 1999: The next-order corrections to quasigeostrophic theory. *J. Atmos. Sci.,* **56,** 1547–1560.

Shearman, R. K., J. A. Barth, J. S. Allen, and R. L. Haney, 2000: Diagnosis of the three-dimensional circulation in mesoscale features with large Rossby number. *J. Phys. Oceanogr.,* **30,** 2687–2709.

Viúdez, A., and D. G. Dritschel, 2003: Vertical velocity in mesoscale geophysical flows. *J. Fluid Mech.,* **483,** 199–223.

——, and ——, 2004: Potential vorticity and the quasigeostrophic and semigeostrophic mesoscale vertical velocity. *J. Phys. Oceanogr.,* **34,** 865–887.

——, R. L. Haney, and J. T. Allen, 2000: A study of the balance of horizontal momentum in a vertical shearing current. *J. Phys. Oceanogr.,* **30,** 572–589.